Impact of freshwater plumes on intraseasonal upper ocean variability in the Bay of Bengal

Channing J. Prend[a,*], Hyodae Seo[b], Robert A. Weller[b], John.T. Farrar[b]

[a] *Scripps Institution of Oceanography, La Jolla, CA, USA*
[b] *Woods Hole Oceanographic Institution, Woods Hole, MA, USA*

A B S T R A C T

The Monsoon Intraseasonal Oscillations (MISO) is known to be strongly coupled to the upper ocean variability in the Bay of Bengal (BoB). Here, we analyze high-resolution moored observations from the northern BoB (18 °N, in comparison with an array of moorings to the south along 90 °E (8, 12, and 15 °N) to examine the observed temperature and salinity variability during the 2015 summer monsoon season. The heat budget analysis indicates that the mixed-layer (ML) temperature tendency at 18 °N in late summer (August and September) deviated greatly from the tendency that is expected based on surface heat flux alone. Examination of moored ML salinity and satellite sea surface salinity (SSS) fields suggests that southward extension of riverine freshwater plumes to the mooring site in late summer plays an important role in modulating the heat balance. The associated shoaling of the ML results in enhanced penetrative heat loss and warming beneath the surface layer. Price-Weller-Pinkel (PWP) 1-D model simulations, which account for vertical mixing, suggest that the entrainment of this subsurface warm water under monsoon wind improves closure of the temperature balance. Long-term analysis of satellite-based sea surface temperature (SST) and rainfall data indicates that late summer ML shoaling is accompanied by amplified intraseasonal (10–60 day) SST variability and reduced MISO precipitation variability. Overall, these results demonstrate the critical importance of freshwater plumes to improved understanding of the upper-ocean heat budget and air-sea interaction in the BoB.

1. Introduction

The boreal summer, defined here as June to September (JJAS), is characterized by southwesterly winds and high precipitation over the Bay of Bengal (BoB, Fig. 1a). This period, known as the Indian Summer Monsoon (ISM; Webster et al., 1998; Wang, 2005), supports air-sea coupling and monsoon rainfall that is particularly enhanced on intraseasonal (10–60 days) time-scales (Yasunari, 1979; 1980; Sikka and Gadgil, 1980; Lawrence and Webster, 2001; Yang et al., 2008). This intraseasonal air-sea interaction is a salient feature for the northward propagating organized convection (Xi et al., 2015; Jongaramrungruang et al., 2017) often referred to as the Monsoon Intraseasonal Oscillations (MISO; Yasunari, 1979; Lee et al., 2013; Webster and Hoyos, 2004; Suhas et al., 2013). Warm sea surface temperature (SST) in the suppressed phase of the MISO, induced by positive shortwave radiation anomaly under calm and clear skies (Girishkumar et al., 2017; Li et al., 2017a, 2017b), precedes the active convection by 7–10 days (Vecchi and Harrison, 2002; Fu et al., 2003; Ajayamohan et al., 2008; Sengupta and Ravichandran, 2001; Han et al., 2006). The resulting cold SST anomalies – driven by reduced solar radiation, enhanced evaporation and turbulent mixing – are known to help create low-level moisture convergences (Hsu and Li, 2012) that, in turn, influence the propagation characteristics of the MISO (Vecchi and Harrison, 2002; Fu et al., 2003; 2004, 2007).

A unique feature in the BoB during the summer monsoon season is the markedly enhanced sea surface salinity (SSS) gradient in the northern and eastern Bay (Fig. 1c). The low SSS in the BoB cannot be explained solely by local evaporation minus precipitation (Sengupta and Ravichandran, 2001; Weller et al., 2016), but is also affected by lateral advection of freshwater input from the Ganges-Brahmaputra-Meghna (GBM) and Irrawaddy river mouths. River discharge accounts for as much as 1.5×10^{12} m^3 yr^{-1} of freshwater into the Bay (Schott et al., 2009; Papa et al., 2010, 2012), making the BoB one of the freshest ocean regions in the tropics (Mahadevan et al., 2016). In particular, intermittent river water intrusions into the northern and central BoB are consistently observed in late summer (August-September; Wu et al., 2007). The corresponding freshwater distribution affects the vertical structure of the upper ocean by shoaling the mixed layer (ML), deepening the isothermal layer depth (ILD) through penetrative solar radiation, and forming a barrier layer (Shetye et al., 1996; Vinayachandran et al., 2002; Thadathil et al., 2007; Jana et al., 2015). Because of the shallow ML and presence of a barrier layer, the upper ocean becomes markedly more responsive to atmospheric forcing (Lukas and Lindstrom, 1991; Vialard and Delecluse 1998; Shenoi et al., 2002; Lucas et al., 2016).

Past studies suggest that during the summer monsoon, surface heat fluxes in the BoB largely account for the intraseasonal variability (ISV) of SST in locations where the ML remains deep (Sengupta and

---

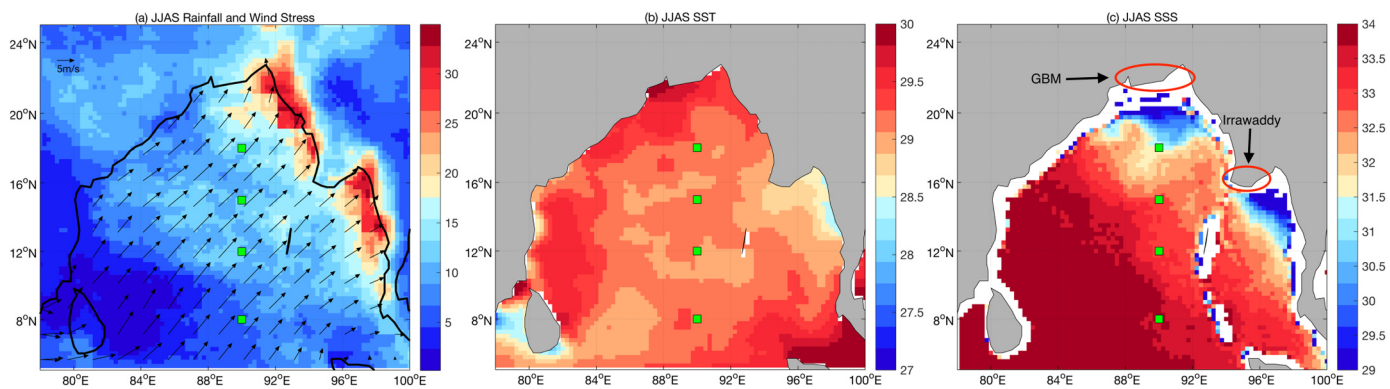**Fig. 1.** Summer (JJAS) 2015 averaged (a) TRMM 3B42 rainfall (mmday^{-1}) overlaid with ASCAT wind vectors (b) NOAA OI SST (°C), and (c) SMAP SSS (psu) with major river mouth locations (Ganges-Brahmaputra-Meghna and Irrawaddy) marked. The WHOI and RAMA mooring locations are denoted by green boxes.

Ravichandran, 2001; Parampil et al., 2010; Sengupta et al., 2016). However, when the ML becomes shallow due to enhanced stratification resulting from river discharges, the 1-D heat balance based on surface heat flux alone tends to be modified by the heat loss associated with solar radiation penetrating the base of the shallow mixed layer and entrainment warming (Sengupta and Ravichandran, 2001; Howden and Murtugudde, 2001; Sengupta et al., 2016). Some modeling studies suggest that the low salinity and shallow MLD enhances intraseasonal SST anomalies (Han et al., 2001; Vinayachandran et al., 2012; Li et al., 2017a, 2017b), which in turn affects the large-scale monsoons (Seo et al., 2009; Vinayachandran et al., 2015).

This study examines the influence of salinity on the ML heat budget using new high-resolution moored observations in the northern BoB (18 °N, 90 °E) from the summer of 2015. Analysis of these observations will be compared to data from the Research Moored Array for African-Asian-Australian Monsoon Analysis and Prediction (RAMA) moorings located further south at 8, 12, 15 °N but along the same meridian (90 °E). Past analysis of the RAMA array suggests that the amplitude of MISO-related variability, as well as the contribution of vertical processes to the ML temperature budget, increases to the north (Girishkumar et al., 2017). This meridional asymmetry will be further examined using the new moored observations, which were collected close to the GBM river mouth. The mooring location is uniquely situated to help clarify how river intrusions affect the ML stratification and heat budget. We will also supplement the analysis of moored observations with satellite and other gridded long-term datasets to investigate the link between the BoB MLD, mediated by the freshwater distribution, and the SST ISV and MISO rainfall variability.

The outline of this paper is as follows. In the next section, observational data sets and methods of analysis are discussed. Section 3 compares the upper ocean variability from the 4 mooring sites. Section 4 discusses the ML heat balance based on the moored observations. Section 5 examines the changes in SST ISV and MISO rainfall variability. This is followed by summary and conclusions in Section 6.

2. Data and methodology

2.1. Moored observations

This study uses high-resolution moored observations from a Woods Hole Oceanographic Institution (WHOI) mooring deployed at 18 °N, 90 °E from December 8, 2014 to January 29, 2016 as part of the Air-Sea Interactions in the Northern Indian Ocean (ASIRI)-Ocean Mixing and Monsoons (OMM) US-India Joint field experiment (Weller et al., 2016; 2018). The mooring measured the upper-ocean temperature, salinity, and velocity fields at high vertical resolution (roughly every 2–6 m in the top 100 m of the water column). Note that the instruments between 32 and 40 m were stripped off the mooring. The mooring also recorded

a full range of surface meteorological variables, from which surface heat, momentum, and freshwater fluxes are estimated using the COARE bulk formula (Fairall et al., 1996, 2003). An overview of the moored system is provided in Weller et al. (2018). For more detail about the system and available dataset, see the WHOI Upper Ocean Process group website (http://uop.whoi.edu/projects/Bengal/Bengal.html).

The three RAMA moorings (http://www.pmel.noaa.gov/tao/drupal/disdel), located in the BoB along 90 °E at 8, 12, and 15 °N (McPhaden et al., 2009), are also analyzed to examine how upper-ocean variability differs at locations further away from the GBM river mouths (Fig. 1c). RAMA data include subsurface salinity and temperature records but at a coarser vertical resolution than the 18 °N mooring, so the corresponding profiles are linearly interpolated to the finer vertical grid. The RAMA data also provide currents and surface meteorology; however the data contain missing fields during the summer of 2015, so satellite and gridded flux datasets are used at the RAMA mooring locations.

In this study, mixed layer depth (MLD) is calculated based on the density criteria following de Boyer Montegut et al. (2007) except with a different threshold value. MLD is defined as the depth at which the change in the potential density (σ_θ) from the surface corresponds to a temperature difference of 0.5 °C, i.e.,

$$\Delta\sigma = \sigma_\theta(T_0-0.5, \; S_0, \; P_0) - \sigma_\theta(T_0, \; S_0, \; P_0), \tag{1}$$

where T_0, S_0, and P_0 are the temperature, salinity, and pressure at the surface. The WHOI mooring data give an average value of $\Delta\sigma = 0.04 \, \mathrm{kg\,m^{-3}}$ over the entire time series, which is used in the rest of this analysis. This $\Delta\sigma$ is similar to values obtained in other studies (Rao and Sivakumar, 2003; Chi et al., 2014; Thangaprakash et al., 2016). The analysis was repeated with various MLD criteria, and the results are largely consistent (not shown).

2.2. Other data products

This study also makes use of daily 8-day running averaged sea surface salinity (SSS) data from the Soil Moisture Active Passive (SMAP) satellite sensors, available on a 0.25 ° × 0.25 ° grid (Mecklenburg et al., 2012, https://podaac-opendap.jpl.nasa.gov/opendap/allData/smap/L3/RSS/V2/8day_running/SCI/), and the Argo monthly gridded near-surface salinity data for 2004–2015 (Riser et al., 2016). Daily surface heat flux estimates are obtained from TropFlux (1 ° × 1 °, Praveen et al., 2012, http://www.incois.gov.in/tropflux_datasets/data/daily/), which is used in the ML heat budget calculations at the RAMA mooring locations. Optimal interpolated (OI) TRMM Microwave Imager (TMI) + Advanced Microwave Scanning Radiometer for EOS (AMSR-E) SST product (0.25 ° × 0.25 °, Wentz et al., 2015, http://www.remss.com/missions/tmi/) is used to estimate the lateral SST gradients around the mooring locations. For consistency, all datasets are linearly interpolated to the 0.25 ° × 0.25 °

SMAP grid. Time series from the mooring data were compared with the satellite measurements when available to ensure the quality of these datasets (Sharma et al., 2016; Weller et al., 2016). The Argo-derived MLD (Holte and Talley, 2009, http://mixedlayer.ucsd.edu) and the daily $0.25° \times 0.25°$ NOAA Optimum Interpolation (OI) SST analysis (Reynolds et al., 2007, https://www.ncdc.noaa.gov/oisst) are used in Section 5.

2.3. Price-Weller-Pinkel model

The Price-Weller-Pinkel (PWP) 1-D ocean model (Price et al., 1986) is used to estimate vertical mixing at 18 °N. The model is initialized from the 18 °N moored temperature and salinity profiles and forced by the surface heat, momentum, and freshwater fluxes recorded or estimated at the mooring. The entrainment takes place when the bulk Richardson number exceeds the threshold value (0.65). Gradient Richardson number mixing, based on a criterion of 0.25, is performed below the MLD. The model uses the Paulson and Simpson double exponential algorithm for calculating penetrative heat flux with constant values of R (0.41), the relative magnitude factor of near-infrared and visible wavelength light, ζ_1 (0.9 m), and ζ_2 (23 m) the optimal attenuation length scales. These values are based on irradiance measurements collected during the past six cruises in the BoB from 2009 to 2014 (Lotliker et al., 2016), and are the same constants used in the moored mixed layer heat budget analysis (Section 4). For this study, we apply a $\Delta\sigma = 0.04\ \mathrm{kg\,m^{-3}}$ MLD criteria to the model output in order to maintain consistency when comparing with the MLD directly estimated from the moorings. It should be noted that PWP does not account for horizontal turbulent fluxes. Therefore, it is not expected to well represent the ML temperature balance when horizontal advection is strong.

3. Freshwater intrusion events

The daily evolutions of SSS, MLD, and SST at the WHOI and three RAMA moorings for the summer of 2015 are presented in Fig. 2. The SSS time-series in the northern Bay shows rapid, high-magnitude fluctuations in August and September (Fig. 2a). The magnitude of variability is greatest at 18 °N (red), which shows three major salinity drops associated with the arrival of freshwater tongues. The 15 °N mooring

(orange) had one large drop in salinity in mid-August, related to the same freshwater tongue that affected 18 °N in early August. Fig. 3 gives spatial maps of SMAP SSS showing the larger-scale propagation of the freshwater plume corresponding to the observed salinity minima at 15 °N and 18 °N. On July 28, the plume becomes just visible off the head of the Bay. By August 3, the fresh tongue has extended southward and almost touches the 18 °N mooring. On August 9, the core of freshest water (< 27 psu) arrives at 18 °N, with the leading edge of the plume reaching nearly 15 °N. Then by August 15, the core has receded, although the plume's shape still leaves a fresh signature that is visible in the SSS distribution north of 15 °N. The river plume in Fig. 3 does not extend far enough south to have any significant effect on the RAMA moorings at 12 °N and 8 °N. This is apparent in the moored SSS (Fig. 2a) at 12 °N (green) and 8 °N (blue), which exhibits much weaker variations compared to 15 °N (orange) and 18 °N (red). The SSS at 8 °N in particular remains the most saline. Comparison between 8 °N and 18 °N illustrates a large north-south contrast in the salinity distribution, which is especially pronounced in late summer.

Fig. 2b shows the corresponding MLD evolutions at each mooring. At 18 °N, the MLD remains deep (10–30 m) in early summer (June-July) and then shoals abruptly to less than 5 m with the arrival of freshwater plumes in late summer (August-September). The MLD quickly deepens as the river plume recedes and the salinity rises, but still remains relatively shallow through October. At 15 °N, there is one major shoaling event around August 15, which coincides with a salinity minimum (orange curve in Fig. 2a). At the 12 °N and 8 °N moorings, the MLD is typically deeper throughout the summer, although the variability can at times be larger. Episodic shoaling events at 8 °N appear unrelated to the river plume-driven MLD variations at the northern moorings (Fig. 2a) and may be related to synoptic wind events. On average, however, the MLD remains shallower in the northern BoB and during the late-summer monsoon.

Fig. 4 shows the 5-day low-pass filtered SSS, MLD, wind stress magnitude (τ), SST, and downward shortwave radiation (Q_{sw}) at 18 °N only. In early summer, the MLD variability at 18 °N is anti-correlated with the wind stress (Fig. 4b). During the late monsoon, however, in addition to the contribution by the wind stress, freshwater intrusion events also act to shoal the MLD. The seasonal climatology of Argo 5 m salinity from 2004 to 2015 (not shown) confirms that the late summer
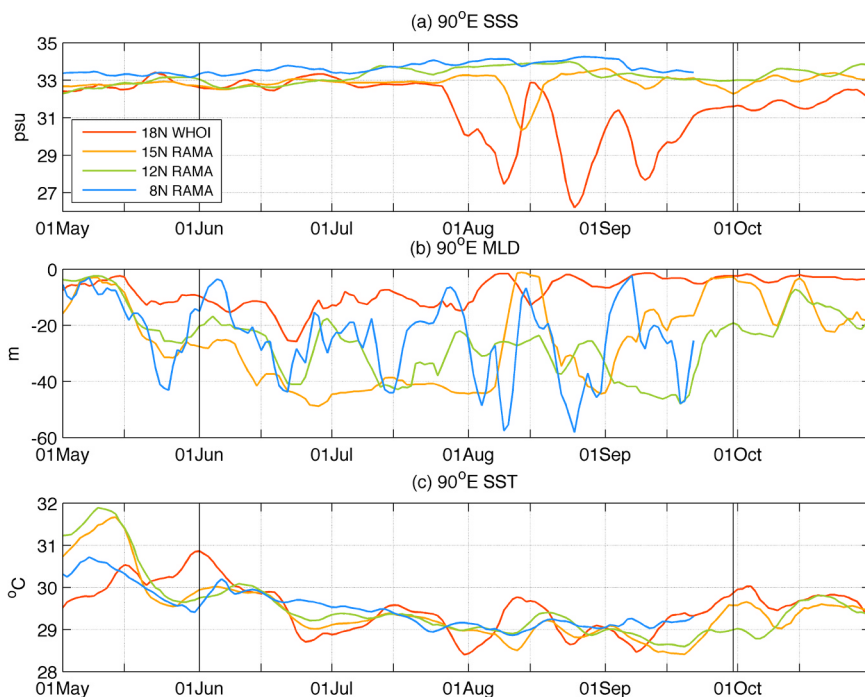

Fig. 2. Observed daily (a) sea surface salinity (SSS, psu), (b) mixed layer depth (MLD, m), and (c) sea surface temperature (SST, °C) from moorings, color-coded to represent the 4 locations along 90 °E. Daily data are shown from May 1 to Oct 31, 2015 after 5-day smoothing. Black vertical lines denote June 1 and September 30, marking the summer monsoon period.
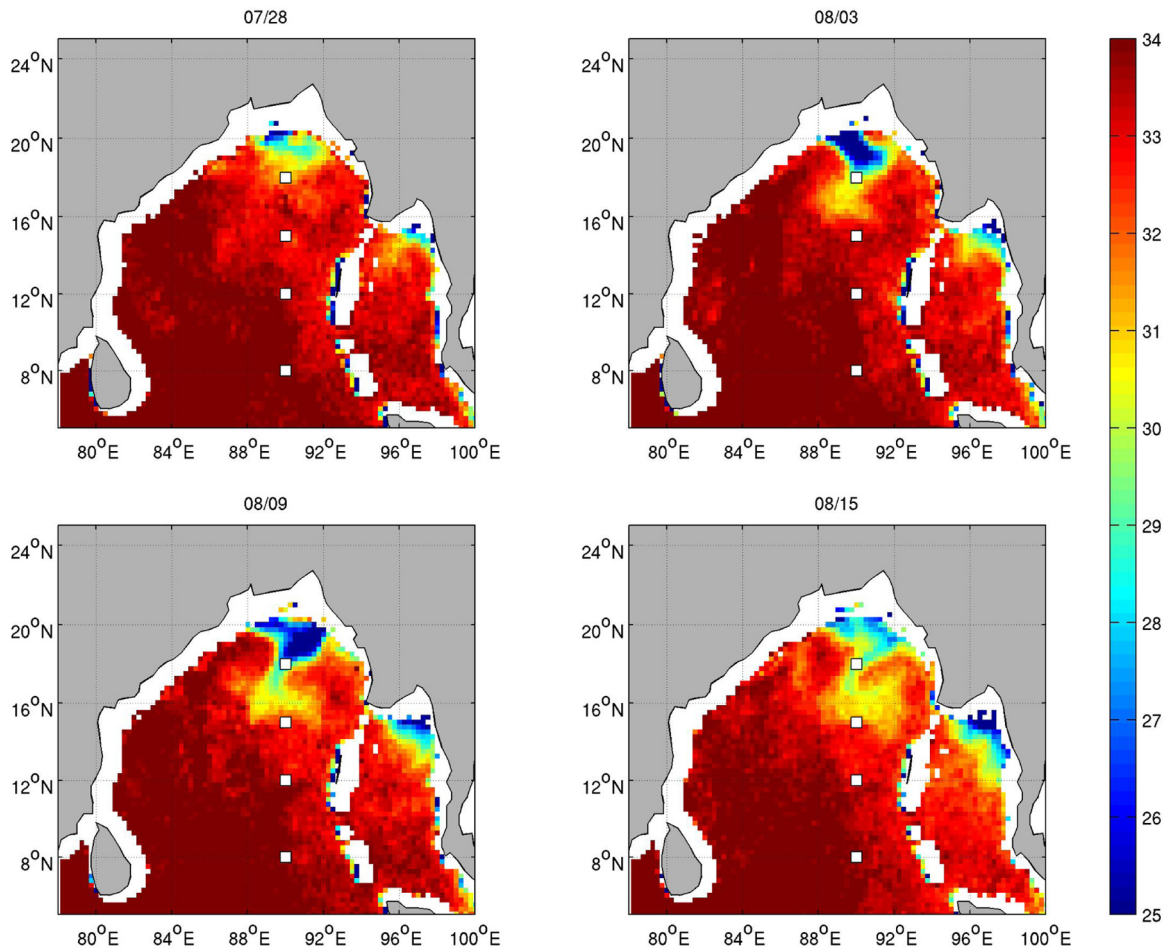
Fig. 3. Snapshots of the SMAP salinity (psu) fields every 6 days showing the arrival of the first freshwater plume to the WHOI mooring location at 90 °E and 18 °N. The white boxes denote the location of the WHOI and RAMA moorings.

freshening in the northern Bay is a robust feature and not a phenomenon unique to 2015. The upper ocean stratification in the northern BoB is modulated by the salinity variability associated with river

discharges, which peak in late summer (Papa et al., 2010; Jana et al., 2015).

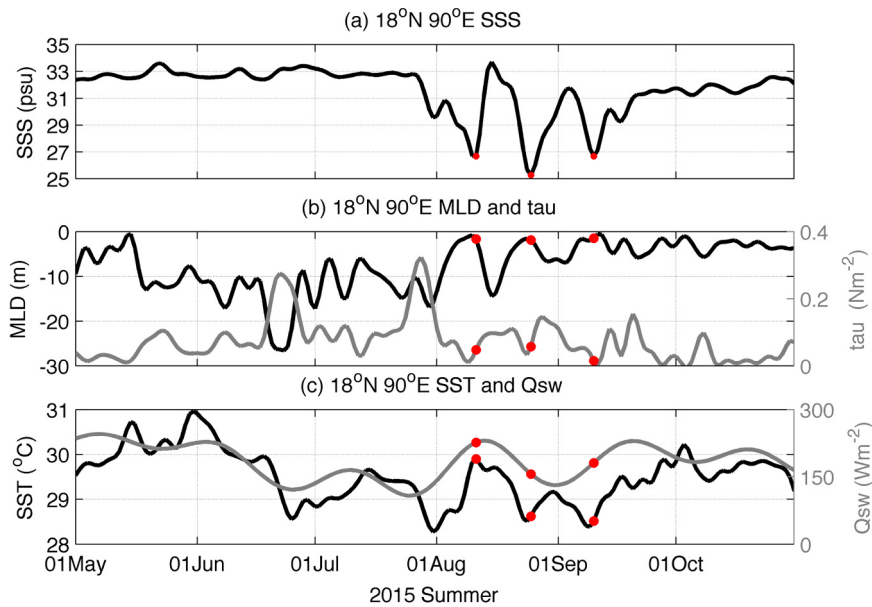The SST evolution observed at 18 °N (Figs. 2c, 4c) shows an SST

Fig. 4. Observed 5-day smoothed upper ocean and flux quantities observed at 18 °N, 90 °E, (a) SSS (psu), (b) MLD (m, black) and wind stress (τ, Nm^{-2}, gray), (c) SST (°C, black) and downward shortwave radiation (Q_{sw}, Wm^{-2}, gray). Red filled circles identical in each of the panels indicate the timing of the three SSS minima.

maximum during the first river intrusion event in early August, and SST minima during the second and third events in late August and early September, respectively. The time series of shortwave radiation (gray) in Fig. 4c, which reflects the large-scale MISO intraseasonal convective variability, shows a maximum Q_{sw} coinciding with the first river intrusion event in early August. Positive intraseasonal Q_{sw} anomalies are associated with the reduced cloud cover that is typical of the suppressed MISO phase (Kembell-Cook and Wang, 2001; Girishkumar et al., 2017). Therefore, this suggests that the first freshwater plume arrived at the mooring during a suppressed phase of MISO convection. On the other hand, the second and the third events took place just before and after the peak of the active MISO phase in early September, as suggested by the coincident Q_{sw} minima. While the SST evolution at 18 °N is largely determined by the downward shortwave radiation flux associated with the intraseasonal MISO variability (Sengupta and Ravichandran, 2001), the size of the SST response can be amplified locally due to the salinity stratification, which supports a shallow MLD. This indicates the role of barrier layer dynamics in increasing the upper ocean response to surface heat fluxes since the enhanced stratification of the water column supports stronger air-sea coupling (Shenoi et al., 2002).

Increasingly strong salinity stratification results in a shallower MLD toward the northern Bay (Fig. 2b). The SST ISV for June-September, which is measured as the standard deviation of 10–60 day band-pass filtered SST using a sixth-order Butterworth filter, also increases with latitude with the maximum at 18 °N (Table 1; Fig. 5). This spatial pattern of SST ISV may not be entirely driven by that of heat flux, especially in the region of high salinity stratification in the northern BoB. Therefore, the freshwater distribution in the BoB, which does display a strong meridional asymmetry, is likely important in determining the SST ISV pattern in response to the large-scale MISO. This is further discussed in Section 5.

4. Mixed layer heat budget analysis

The salinity distribution in the BoB exhibits distinct geographical and sub-seasonal contrasts. This section examines how such freshwater distributions affect the ML heat budget. A ML heat budget is calculated for the WHOI and RAMA moorings following Sengupta and Ravichandran (2001), Chi et al. (2014), Thangaprakash et al. (2016), and Girishkumar et al. (2017) as

$$\frac{\partial T}{\partial t} = \frac{Q_{eff}}{\rho_w C_p h} - \left[\left(u\frac{\partial T}{\partial x} + v\frac{\partial T}{\partial y} \right) + H\left(W_h + \frac{\partial h}{\partial t} \right)\frac{(T - T_h)}{h} \right] + \text{Residual.}$$
(2)

where C_p is the heat capacity (4185 J kg^{-1} °C^{-1}), and h the mixed layer depth. The terms in brackets in represent, from left to right, zonal and meridional advection, vertical entrainment, and heat flux into the ML from below. W_h is the vertical velocity, which is combined with the rate of change of MLD ($\partial h/\partial t$) to give the entrainment velocity. H is the Heaviside step function, where H = 0 when $W_h + \partial h/\partial t$ is negative and

H = 1 when positive. Finally, the residual term includes diffusion, numerical errors due to finite differencing and other unresolved processes. $Q_{eff} = Q_{net} - Q_{pen}$ is the effective heat absorbed by the ML, calculated by subtracting penetrative shortwave radiation (Q_{pen}) from the net surface heat flux Q_{net} (the sum of short and longwave fluxes and latent and sensible heat fluxes). The Paulson and Simpson (1977) double exponential model is applied to estimate the amount of penetrative heat flux,

$$Q_{pen} = Q_{sw}\left[\text{Re}^{\frac{-h}{\zeta_1}} + (1 - R)e^{\frac{-h}{\zeta_2}} \right].$$
(3)

where Q_{sw} is the shortwave radiation, R is the relative magnitude factor of near-infrared and visible wavelength light, h is the mixed layer depth, and ζ_1 and ζ_2 are the optimal attenuation length scales. As noted earlier, constant values for R (0.41), ζ_1 (0.9 m), ζ_2 (23 m) are used based on irradiance measurements collected during the past six cruises in the BoB from 2009 to 2014 (Lotliker et al., 2016). It is important to take into account Q_{pen} since the shallow MLD allows much of the heat to penetrate below the ML with little contribution to the ML heating (Sengupta and Ravichandran, 2001). The simplified 1-D balance, in which the advection and vertical mixing terms are ignored and thus Q_{eff} alone balances temperature tendency, can be expressed as:

$$\frac{\partial T}{\partial t} = \frac{Q_{eff}}{\rho C_p h}.$$
(4)

The Q_{eff}–based 1-D balance is calculated at 18 °N using Q_{net} obtained from the telemetered meteorological measurements using the COARE bulk formula (Fairall et al., 2003). The RAMA mooring data had many gaps in the fields necessary to compute surface fluxes, so the Q_{net} from TropFlux are used at the respective mooring locations. For all moorings, MLD (h) is found using a 0.04 kg m^{-3} density threshold.

The accuracy of the simple 1-D heat balance at each of the mooring locations is assessed via correlation between the observed and estimated temperature tendency. The correlation is calculated for the 10-day low-pass filtered temperature tendency observed and estimated by Eq. (4) during JJAS in 2015. The correlation values are then plotted as a function of latitude with error bars denoting the standard errors. Fig. 6a shows that the 1-D prediction improves as the latitude decreases. Significant (p = 0.01) positive correlations exceeding 0.5 are found at the three RAMA moorings, while at the WHOI mooring, the correlation is distinctively low (0.28, still significant at the 95% confidence level). The reduced correlation at 18 °N suggests that another process is needed to account for the observed temperature tendency.

A closer examination of the WHOI mooring heat budget shows that the 1-D balance based on Q_{eff} alone breaks down only in late summer. Fig. 6b shows scatterplots of the 10-day low-pass filtered observed temperature tendency and temperature tendency predicted by the Q_{eff}–based 1-D heat balance. In early summer (blue), there is a correlation of 0.60 between the observations and simple 1-D balance, which is comparable to values from the RAMA moorings. In late summer (orange), however, the Q_{eff}–based 1-D balance over-estimates the cooling, showing a weak and insignificant (p = 0.01) correlation coefficient with the observations. Given that the observed cooling was weaker than expected from the heat flux alone, other processes must act to warm the mixed layer.

Results of the 1-D calculation for the 18 °N mooring in August and September are summarized in Fig. 7. The time series are 10-day low-pass filtered to suppress high-frequency variability. The observed ML temperature tendency (orange) and the temperature tendency predicted by Q_{eff} alone (blue) do not match well in late summer. Therefore, the PWP model is used to estimate vertical entrainment. The model is initialized with temperature and salinity profiles observed at 18 °N on July 31, 2015. It is clear from Fig. 7 that the temperature tendency calculated from the PWP model (green) matches the observations (orange) better than the Q_{eff}–based tendency (blue). In particular, the two

Table 1
SST intraseasonal variability (ISV) at the 4 mooring locations along 90 °E for the 2015 summer monsoon season (June-September). The SST ISV is calculated as the standard deviation of 10–60 day band-pass filtered SST using a sixth-order Butterworth filter. Note that at the 8 °N RAMA mooring, the SST record ends on September 21, so the standard deviation is calculated for the period of May 1 to Sep 21 only.

Latitude (°N)	SST ISV (°C)
18	0.39
15	0.29
12	0.26
8	0.08

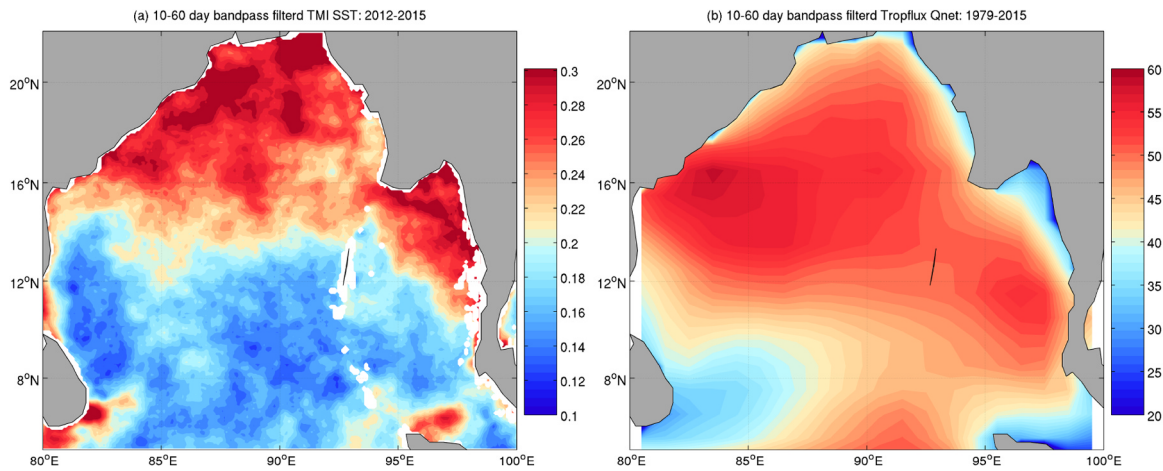**Fig. 5.** Maps of JJAS intraseasonal (10–60 day) standard deviation of (a) TMI SST (°C) for the period of 2012–2017 and (b) Tropflux Qnet (W/m2) for the period of 1979–2017.

spurious cooling events predicted by the surface heat flux are completely removed in the PWP model calculation. These predicted cooling events coincide with the second and third river intrusions that occurred during the active phase of the MISO (Fig. 4). The shoaling of the ML associated with the river intrusions allows greater penetrative solar radiation. In the absence of wind stress, penetrative heat loss over a shallow ML would result in cooling of the ML temperature. However, under even moderate monsoon wind stress (Fig. 4b), wind-driven vertical mixing can allow the warm water within the IL but below the ML to be entrained into the ML. This effect is missing in the 1-D balance based on Q_{eff} alone, allowing the spurious cooling events to take place.

The PWP model simulations, therefore, suggest that the entrainment of this subsurface warm water is essential for the accurate description of the ML temperature evolution. Note that the simple Q_{eff}–based 1-D balance remains skillful during the first river intrusion event in early August, which occurred under the suppressed phase of the MISO when the entrainment velocity is perhaps small (Eq. (2)). For completeness, the lateral temperature advection terms are also estimated using zonal and meridional currents recorded at 4-m depth from the 18 °N mooring in combination with daily SST gradients estimated from TMI + AMSR-E. Fig. 7 (purple) shows that taking into account horizontal temperature advection in addition to the PWP model has only a minor effect in improving the heat budget in comparison to the PWP model alone (green). It is speculated that this is because SST gradients in the BoB
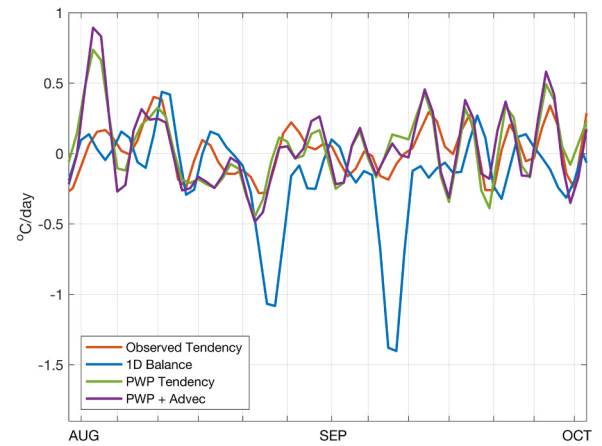

Fig. 7. Time series of 10-day low-pass filtered temperature tendency (°Cday^{-1}) at 18 °N for late summer (August-September) in 2015 from (orange) the observations, (blue) the 1-D heat balance, (green) the PWP model, and (purple) the PWP model plus horizontal advection. The PWP model is initialized July 31 for the simulation of late summer.
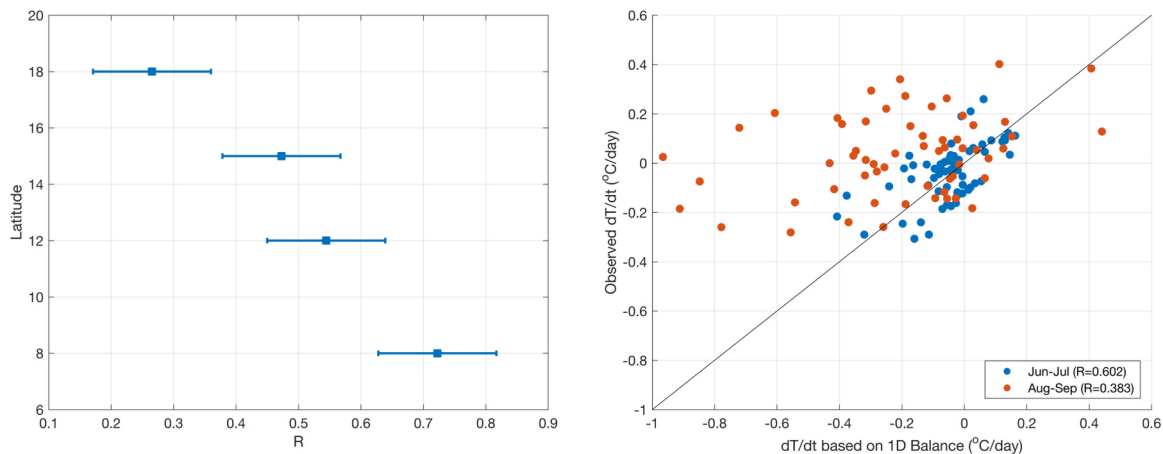

Fig. 6. (a) Correlation coefficient of 10-day low-pass filtered temperature tendency between the observations and the tendency predicted by surface heat flux as a function of latitude at the WHOI and RAMA mooring locations. The error bars denote the standard errors. (b) Scatter plots of the 10-day low-pass filtered temperature tendency (°Cday^{-1}) from the observations and the 1-D heat balance at the 18 °N mooring location for early summer (June-July) in red and late summer (August-September) in blue. Points on the black line (y = x) are when the 1-D balance matches the observations.
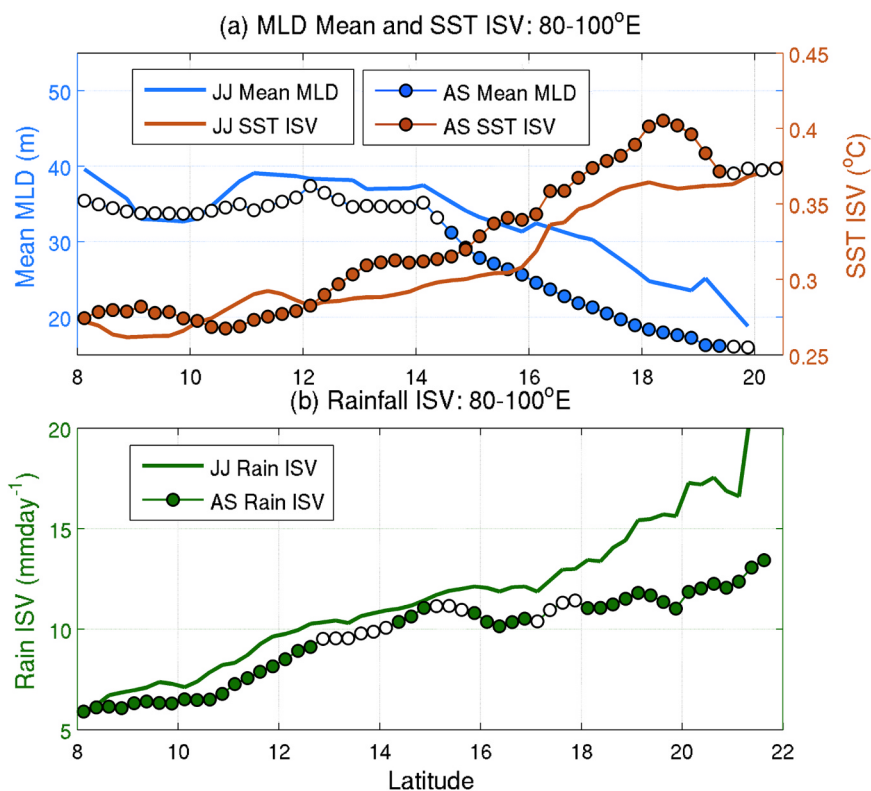
(a) MLD Mean and SST ISV: 80-100°E

(b) Rainfall ISV: 80-100°E

Fig. 8. (a) (Left axis, blue) June-July (solid) and August-September (solid line with filled/closed circles) MLD (m) averaged over the BOB (80–100 °E). The MLD estimate is based on Holte and Talley (2009) for the period of 2005–2017. Filled circles denote the areas where the time-mean differences in MLD between June-July and August-September are significantly different at the 95% confidence level. (Right axis) Brown curves compare the level of intraseasonal variability (ISV) of SST, determined by the standard deviation of 10–60 day bandpass filtered NOAA OI SST dataset for the period of 2005–2017. Filled circles denote that the SST ISVs in June-July is significantly different from that in August-September at the 95% confidence level. (b) As in SST in (a) except for comparing the difference in rainfall ISV based on TRMM3B42 precipitation estimate for the period of 2005–2017.

during summer are typically small (Fig. 1b).

5. Link with SST ISV and MISO rainfall variability

The analysis of moored observations and satellite data highlight the marked geographical and subseasonal contrasts of ML stratification and heat balance. This section explores how such variabilities might be related to the long-term ISV characteristics of SST and monsoon rainfall. The left axis of Fig. 8a shows the zonally averaged (over BoB, 80–100 °E) MLD from Holte and Talley (2009) from 2005 to 2017. The solid blue line denotes the meridional profile of the MLD values at 1° intervals as a function of latitude averaged in early summer (June-July), while the blue line with filled/open circles represents the MLD profile averaged in late summer (August-September). The filled circles represent the locations where the time-mean difference in MLD between early and late summers is significantly different at the 95% confidence level, which is determined based on the two-sided *t*-test. On the right axis, SST ISV is superposed for early summer (solid brown line) and late summer (the brown line with filled/open circles). To obtain the SST ISV values, a 10–60 day band-pass filter using a sixth-order Butterworth filter has been applied to full-year daily SST data first (with the seasonal cycle removed), after which the June-July and August-September values are extracted to calculate the standard deviation and then zonally averaged. The F-test is used to determine where the SST ISV (i.e., the standard deviation of 10–60 day band-pass filtered SST) between early and late summer is significantly different at the 95% confidence level.

There is an inverse relationship between the time-mean MLD and SST ISV as a function of latitude in both early and late summers. Climatologically, the MLD becomes increasingly shallow toward the north. In particular, it is much shallower in late summer compared to early summer, especially over the 16–20 °N range (the northern BoB). This is consistent with Figs. 2–4, and further demonstrates the importance of freshwater intrusions to the northern BoB stratification. Conversely, SST ISV is gradually enhanced toward the north, with statistically significant increase apparent in late summer and north of

15 °N. The result is insensitive to the choice of different filtering scales, the period of data, and zonal averaging (not shown), which suggests that the late summer enhancement of the SST ISV in the northern BoB is a robust feature.

How would changes in time-mean MLD and SST ISV be related to the MISO intraseasonal rainfall variability? In Fig. 8b, the solid green curve denotes the 10–60 day bandpass filtered rainfall standard deviation (rainfall ISV) in early summer, which is to be compared with that in late summer (the green solid line with filled/open circles). The MISO rainfall variability is obtained in the same way as the SST ISV considering the precipitation only over the oceanic grid points. Statistically, the MISO rainfall variability in late summer is significantly reduced compared to early summer. Furthermore, this difference becomes increasingly apparent toward the northern BoB. Previous studies suggest that the SST ISV is largely induced by the atmospheric ISV in rainfall and wind (Sengupta and Ravichandran, 2001; Han et al., 2006). However, in the northern BoB, this contradicts our observation that SST ISV increases while the rainfall ISV subsides. It is hypothesized that this is related to the reduced mean wind and rainfall from early to late summers, which is a part of the intrinsic seasonal cycle of the tropical atmosphere (e.g. Kembell-Cook and Wang, 2001). Reduced mean wind would erode the barrier layer less, and therefore, for a given change in rainfall (or wind) ISV, the SST ISV response can be amplified. Testing this hypothesis is, however, difficult with observations alone, and a modeling study is currently underway. The results will be reported elsewhere.

6. Summary and conclusion

The northern BoB is a unique region to study air-sea interactions as river inputs play a large role in driving ML stratification and temperature variability. This study uses moored observations from 4 locations in the BoB to examine upper ocean variability during the 2015 summer monsoon season. Through ML heat budget analyses, we find that the simple 1-D temperature balance based on Q_{eff} alone largely holds for the southern mooring sites and during the early summer

monsoon (June-July) in the northern Bay. At 18°N during the late monsoon (August-September) however, the Q_{eff}–based 1-D balance is no longer valid. This period coincided with the southward propagation of several freshwater plumes to the mooring site (Sree Lekha et al., 2018). The strong salinity stratification associated with river water intrusions supports an extremely shallow MLD and large penetrative solar radiation, leading to subsurface warming and a deep ILD. When a shallow MLD and deep ILD occurs under the active phase of MISO convection, as was observed in the second and third river intrusion events in late August and early September (Figs. 2–3), the entrainment warming from below the ML becomes crucial in explaining the observed temperature tendency.

In contrast, despite the shallow ML during the first river intrusion in early August, this event coincided with a peak in the suppressed phase of MISO convection and weak entrainment velocity, and therefore the 1-D budget based only on surface heat flux was able to accurately account for the observed ML temperature tendency. This MISO-phase dependent role of vertical mixing in the ML heat budget is confirmed by Price-Weller-Pinkel (PWP) model simulations, which greatly improved the skill of the 1-D heat budget in late summer. The salt budget analysis (not shown) also revealed that the large salinity gradients associated with the freshwater plumes cause horizontal advection to dominate the SSS variability in August and September. These results suggest that freshwater intrusions under active MISO phases play a critical role in the ML heat budget in the northern BoB, especially during late summer.

Comparison of long-term MLD and SST datasets reveals that SST ISV is significantly enhanced north of 15°N in late summer, coinciding with a shoaling of the climatological MLD. This implies that the enhanced ML stratification in late summer amplifies the SST ISV, which is consistent with the role of the barrier layer (Shenoi et al., 2002). Furthermore, there is some indication that the increased SST ISV in the northern BoB during late summer concurs with a statistically significant decrease in the MISO rainfall ISV. Whether or not the decreased MISO rainfall activity arises from the enhanced SST ISV or merely reflects the MISO subseasonal cycle internal to the atmosphere (Kembell-Cook and Wang, 2001) cannot be determined from this study using the observations alone and is left as a future goal.

Acknowledgement

References

Chi, N.-H., Lien, R.-C., D'Asaro, E.A., Ma, B.M., 2014. The surface mixed layer heat budget from mooring observations in the central Indian Ocean during Madden-Julian Oscillation events. J. Geophys. Res. Oceans 119, 4638–4652.

de Boyer Montegut, C., Mignot, J., Lazar, A., Cravatte, S., 2007. Control of salinity on the mixed layer depth in the world ocean: 1. general description. J. Geophys. Res. 112, C06011.

Fairall, C.W., Bradley, E.F., Rogers, D.P., Edson, J.D., Young, G.S., 1996. Bulk parameterization of air-sea fluxes for tropical ocean global atmosphere coupled-ocean atmosphere response experiment. J. Geophys. Res. 15, 3747–3764.

Fairall, C., Bradley, E.F., Hare, J., Grachev, A., Edson, J., 2003. Bulk parameterization of air-sea fluxes: updates and verification for the COARE algorithm. J. Clim. 16, 571–591.

Fu, X., Wang, B., Li, T., et al., 2003. Coupling between northward-propagating, intraseasonal oscillations and sea surface temperature in the Indian Ocean. J. Atmos. Sci. 60, 1733–1753.

Girishkumar, M.S., Joseph, J., Thangaprakash, V.P., Pottapinjara, V., McPhaden, M.J., 2017. Mixed layer temperature budget for the northward propagating summer monsoon intraseasonal oscillation (MISO) in the central Bay of Bengal. J. Geophys. Res. Oceans 122, 8841–8854.

Han, W., McCreary Jr., J.P., Kohler, K.E., 2001. Influence of precipitation minus evaporation and Bay of Bengal rivers on dynamics, thermodynamics, and mixed-layer physics in the upper Indian Ocean. J. Geophys. Res 106, 6895–6916.

Han, W., Liu, W.T., Lin, J., 2006. Impact of atmospheric submonthly oscillations on sea surface temperature of the tropical Indian Ocean. Geophys. Res. Lett. 33, L03609.

Howden, S., Murtugudde, R., 2001. Effects of river inputs into the Bay of Bengal. J. Geophys. Res. 106 (No. C9), 19,825–19,843.

Hsu, P.-C., Li, T., 2012. Role of the boundary layer moisture asymmetry in causing the eastward propagation of the Madden-Julian Oscillation. J. Clim. 25, 4914–4931.

Lawrence, D.M., Webster, P.J., 2001. Interannual variations of the intraseasonal oscillation in the south Asian summer monsoon region. J. Clim. 14, 2910–2922.

Lekha, Sree, et al., 2018. Subseasonal dispersal of freshwater in the northern Bay of Bengal in the 2013 summer monsoon season. J. Geophys. Res. 123, 1–19.

Li, Y., Han, W., Ravichandran, M., Wang, W., Shinoda, T., Lee, T., 2017a. Bay of Bengal salinity stratification and Indian summer monsoon intraseasonal oscillation: 1. intraseasonal variability and causes. J. Geophys. Res. Oceans 122, 4291–4311.

Li, Y., Han, W., Wang, W., Ravichandran, M., Lee, T., Shinoda, T., 2017b. Bay of Bengal salinity stratification and Indian summer monsoon intraseasonal oscillation: 2. Impact on SST and convection. J. Geophys. Res. Oceans 122, 4312–4328.

Lotliker, A.A., Omand, M.M., Lucas, A.J., Laney, S.R., Mahadevan, A., Ravichandran, M., 2016. Penetrative radiative flux in the Bay of Bengal. Oceanography 29, 214–221.

Lukas, Roger, Lindstrom, Eric, 1991. The mixed layer of the western equatorial Pacific Ocean. J. Geophys. Res. 96 (Supplement), 3343–3357.

Mahadevan, A., Spiro Jaeger, G., Freilich, M., Omand, M., Shroyer, E.L., Sengupta, D., 2016. Freshwater in the Bay of Bengal: its Fate and Role in Air-sea Heat Exchange. Oceanography 29, 72–81.

McPhaden, M.J., et al., 2009. RAMA, the research moored array for African-Asian-Australian monsoon analysis and prediction: a new moored buoy array in the historically data-sparse Indian Ocean provides measurements to advance monsoon research and forecasting. Bull. Am. Meteorol. Soc. 90, 459–480.

Mecklenburg, S., et al., 2012. ESA's soil moisture and ocean salinity mission: mission performance and operations. IEEE Trans. Geosci. Remote Sens. 50 (5), 1354–1366.

Papa, F., Durand, F., Rossow, W., Rahman, A., Bala, S., 2010. Satellite altimeter-derived monthly discharge of the Ganga-Brahmaputra River and its seasonal to interannual variations from 1993 to 2008. J. Geophys. Res. 115, C12013.

Parampil, S.R., Gera, A., Ravichandran, M., Sengupta, D., 2010. Intraseasonal response of mixed layer temperature and salinity in the Bay of Bengal to heat and freshwater flux. J. Geophys. Res. 115, C05002.

Paulson, C., Simpson, J.J., 1977. Irradiance measurements in the upper ocean. J. Phys. Oceanogr. 7, 952–956.

Praveen, K.B., Vialard, J., Lengaigne, M., Murty, V.S.N., McPhaden, M.J., 2012. TropFlux: air-sea fluxes for the global tropical oceans – description and evaluation. Clim. Dyn. 38, 1521–1543.

Price, J.F., Weller, R.A., Pinkel, R., 1986. Diurnal cycling: observations and models of the upper ocean response to diurnal heating, cooling, and wind mixing. J. Geophys. Res. 91, 8411–8427.

Rao, R.R., Sivakumar, R., 2003. Seasonal variability of sea surface salinity and salt budget of the mixed layer of the north Indian Ocean. J. Geophys. Res. 108 (No. C1), 3009.

Riser, S.C., et al., 2016. Fifteen years of ocean observations with the global Argo array. Nat. Clim. Change 6, 145–153.

Schott, F.A., Xie, S.P., McCreary Jr., J.P., 2009. Indian Ocean circulation and climate variability. Rev. Geophys. 47, RG1002.

Seo, H., Xie, S.P., Murtugudde, R., Jochum, M., Miller, A.J., 2009. Seasonal effects of the Bay of Bengal barrier layer dynamics in a regional coupled model. J. Clim. 22, 6577–6596.

Sengupta, D., Ravichandran, M., 2001. Oscillations of Bay of Bengal sea surface temperature during the 1998 summer monsoon. Geophys. Res. Lett. 28 (10), 2033–2036.

Sengupta, D., Bharath Raj, G.N., Ravichandran, M., Sree Lekha, J., Papa, F., 2016. Near-surface salinity and stratification in the north Bay of Bengal from moored observations. Geophys. Res. Lett. 43, 4448–4456.

Shenoi, S.S.C., Shankar, D., Shetyer, S.R., 2002. Differences in heat budgets of the near-surface Arabian Sea and Bay of Bengal: Implications for the summer monsoon. J. Geophys. Res. 107, 1–14.

Suhas, E., Neena, J.M., Goswami, B.N., 2013. An Indian monsoon intraseasonal oscillations (MISO) index for real time monitoring and forecast verification. Clim. Dyn. 40, 2605–2616.

Thadathil, P., Muraleedharan, P.M., Rao, R.R., Somayajulu, Y.K., Reddy, G.V., Ravichandran, C., 2007. Observed seasonal variability of barrier layer in the Bay of Bengal. J. Geophys. Res. 112.

Thangaprakash, V.P., Girishkumar, M.S., Suprit, K., Suresh Kumar, N., Chaudhuri, D., Dinesh, K., Kumar, A., Shivaprasad, S., Ravichandran, M., Farrar, J.T., Sundar, R., Weller, R.A., 2016. What controls seasonal evolution of sea surface temperature in the Bay of Bengal? Mixed layer heat budget analysis using moored buoy observations along 90˚E. Oceanography 29, 202–213.

Vecchi, Gabriel, Harrison, D.E., 2002. Monsoon breaks and subseasonal sea surface temperature variability in the Bay of Bengal. J. Clim. 15, 1485–1493.

Vinayachandran, P.N., Murty, V.S.N., Ramesh Babu, V., 2002. Observations of barrier layer formation in the Bay of Bengal during summer monsoon. J. Geophys. Res. 107, C08018.

Webster, P.J., et al., 1998. Monsoons: processes, predictability, and the prospects for prediction. J. Geophys. Res. 103 (14), 451.

Weller, R.A., Farrar, J.T., Prend, C.J., Seo, H., Sengupta, D., Ravichandran, M., Venkatsen,

R.2018. Moored observations of upper-ocean response to surface meteorology and air-sea fluxes in the northern Bay of Bengal in 2015, J. Climate, in revision.

Weller, R.A., Farrar, J.T., Buckley, J., Mathew, S., Venkatesan, R., Lekha, S., Dipanjan, Kumar, N.S., Kumar, N.P., 2016. Air-sea interaction in the Bay of Bengal. Oceanography 29, 28–37.

Wentz, F.J., Gentemann, C., Hilburn, K.A., 2015. Remote sensing systems TRMM TMI Daily Environmental Suite on 0.25 deg grid, Version 7.1. Remote Sensing Systems, Santa Rosa, CA (Available online at). ⟨www.remss.com/missions/tmi⟩.

Wu, L., Wang, F., Yuan, D., Cui, M., 2007. Evolution of freshwater plumes and salinity fronts in the northern Bay of Bengal. J. Geophys. Res. 112, C08017.

Yang, B., Fu, X., Wang, B., 2008. Atmosphere-ocean conditions jointly guide convection of the Boreal Summer Intraseasonal Oscillation: satellite observations. J. Geophys. Res. 113, D11105.